Internal wave and boundary current generation by tidal flow over topography

Amadeus Dettner, Harry L. Swinney, and M. S. Paoletti

Citation: Physics of Fluids (1994-present) **25**, 116601 (2013); doi: 10.1063/1.4826984
View online: http://dx.doi.org/10.1063/1.4826984
View Table of Contents: http://scitation.aip.org/content/aip/journal/pof2/25/11?ver=pdfcov
Published by the AIP Publishing

PHYSICS OF FLUIDS **25**, 116601 (2013)

Internal wave and boundary current generation by tidal flow over topography

Amadeus Dettner, Harry L. Swinney,[a] and M. S. Paoletti[b]
Department of Physics and Center for Nonlinear Dynamics, University of Texas at Austin, Austin, Texas 78712, USA

(Received 31 May 2013; accepted 10 October 2013; published online 1 November 2013)

The relationship between boundary currents generated by tidal flow over topography and the radiated internal wave power is examined in two-dimensional numerical simulations of a uniformly stratified fluid. The radiated power P_{IW} and kinetic energy density of the boundary currents are computed as a function of the internal wave slope S_{IW} and the criticality parameter ϵ (ratio of the maximum topographic slope to S_{IW}). Both S_{IW} and ϵ are varied two orders of magnitude about unity by changing the tidal frequency, stratification, or topographic shape and slope. We consider cases where the hydrostatic approximation is valid ($S_{IW} \ll 1$), as well as test theoretical predictions for models of the deep ocean where the beam slope diverges and the hydrostatic approximation fails. We confirm that resonant boundary currents characterized by large kinetic energy densities form over critical topography ($\epsilon = 1$). However, we find that this resonance phenomenon does not extend to the power radiated by internal waves that propagate away from the topography. Further, by directly comparing the kinetic energy density to the energy flux of the generated internal waves, we find that the more easily measured kinetic energy density cannot be used as a proxy to characterize the conversion of tidal energy to radiated internal wave power. Whether the hydrostatic approximation is valid or fails, our measurements of the radiated power can be described as $P_{IW} = P_{tide} f(\epsilon, \text{shape})/S_{IW}$, where P_{tide} is the effective tidal power that interacts with the topography, and $\pi/8 < f(\epsilon, \text{shape}) < \pi/4$ is bounded below by the theoretical prediction of Bell ["Topographically generated internal waves in the open ocean," J. Geophys. Res. **80**, 320–327 (1975)] for $\epsilon \to 0$ and above by Llewellyn Smith and Young ["Tidal conversion at a very steep ridge," J. Fluid Mech. **495**, 175–191 (2003)] for $\epsilon \to \infty$. © *2013 AIP Publishing LLC*. [http://dx.doi.org/10.1063/1.4826984]

I. INTRODUCTION

Internal waves play an important role in the global ocean energy budget by providing mixing necessary to maintain the thermohaline circulation.[1] Approximately half of the internal wave energy in the ocean is produced by tidal flow over topography, resulting in waves at the tidal frequency, known as internal tides. Conversion of the barotropic tide into internal tides occurs at continental slopes,[2–4] sea-mounts,[5,6] ridges,[7,8] and rough topography in the deep ocean.[9,10] An understanding of the efficiency of this conversion is needed to understand the energy budget of the oceans. Therefore, it is useful to measure the total power P_{IW} converted from barotropic tidal motions over topography into radiated internal waves,

$$P_{IW} = \int\int \mathbf{\Phi} \cdot \hat{\boldsymbol{n}}\, ds, \tag{1}$$

[a] swinney@chaos.utexas.edu
[b] mpaoletti@chaos.utexas.edu

where $\mathbf{\Phi} = \langle p'\boldsymbol{v}' \rangle$ is the baroclinic energy flux, p' and $\boldsymbol{v}'$ are, respectively, pressure and velocity perturbations, and brackets $\langle\rangle$ indicate an average over tidal period. The integral is over a surface that contains the topography; $\hat{\boldsymbol{n}}$ is a unit vector normal to this surface. The radiated power P_{IW} generated by tidal flow over two-dimensional topography of height H and extent L_y in the horizontal direction orthogonal to the tidal flow, $v_{\mathrm{tide}} = \hat{\boldsymbol{x}} A\omega \cos \omega t$, may be compared to the effective tidal power that interacts with the topography. We define the effective tidal power by multiplying the maximum tidal energy flux, $\mathbf{\Phi}_{\mathrm{tide}} = \hat{\boldsymbol{x}} \rho_0 A^2 \omega^3 H$ ($\rho_0 A\omega^2 H$ gives the pressure scale and $A\omega$ the velocity scale, where ρ_0 is a reference density), by the effective cross-sectional area of the topography HL_y, obtaining

$$P_{\mathrm{tide}} = HL_y \Phi_{\mathrm{tide}} = \rho_0 H^2 A^2 \omega^3 L_y. \tag{2}$$

We are interested in the conversion of tidal energy into internal wave power, which we characterize as the ratio of the radiated internal wave power P_{IW} to the effective tidal power P_{tide},

$$\widetilde{P} = P_{\mathrm{IW}}/P_{\mathrm{tide}}. \tag{3}$$

In addition to radiating internal waves, barotropic tidal motions over bottom topography produce boundary layer currents. These currents can vary with the topographic steepness, which is characterized by the criticality parameter

$$\epsilon = S_{\mathrm{topo}}/S_{\mathrm{IW}}, \tag{4}$$

where S_{topo} is the maximum topographic slope and $S_{\mathrm{IW}} = \sqrt{\omega^2/(N^2 - \omega^2)}$ (in the absence of rotation) is the slope of the internal waves, where $N(z) = \sqrt{-(g/\rho_0)(d\rho/dz)}$ is the buoyancy frequency for a fluid of density $\rho(z)$ with gravitational acceleration g. Resonant boundary currents are known to form over critical topography ($\epsilon = 1$), where the local topographic slope matches the local slope of the internal wave beams. This resonance phenomenon has been thought to carry over to the resonant generation of internal waves as well by such critical topography. There have been extensive theoretical, experimental, and computational studies of the generation of both boundary currents and internal waves by tidal flow over topography, as reviewed in Sec. II. Here, we examine the relation between the radiated far-field internal wave power to the boundary current intensity, a relationship that has not been explored in previous work.

A number of past studies (see Sec. II) have examined the conversion of barotropic tidal motions to internal tides by two-dimensional topography in the hydrostatic approximation, which assumes that horizontal length scales far exceed vertical length scales. This approximation is appropriate for the strongly stratified shallow ocean, where the local buoyancy frequency $N(z)$ is much greater than the tidal frequency ω. However, King *et al.*[11] found that in the deep ocean the buoyancy frequency can become comparable to or even less than the semi-diurnal lunar tidal frequency $\omega_{\mathrm{M2}} = 1.4052 \times 10^{-4}$ rad s^{-1} for depths greater than about 4 km. As an example, measurements from the Venezuelan Basin (see Fig. 1) show that below about 4 km depth the local buoyancy frequency is less than ω_{M2}.

To investigate the relation of the radiated internal wave power to the corresponding boundary current strength, and also the consequences of weak stratification where the hydrostatic approximation fails, we conduct two-dimensional numerical simulations of the Navier-Stokes equations for tidal flow of a uniformly stratified fluid ($N = \mathrm{const}$) over triangular, Gaussian, knife-edge, and semi-circular topographies. We vary the ratio of the tidal frequency ω to the buoyancy frequency N from values comparable to unity, where nonhydrostatic effects are expected to be significant, to values an order of magnitude smaller, where our measurements may be directly compared with prior hydrostatic theory. We examine the scalings and interplay of the radiated internal wave power and the boundary currents by independently varying the tidal frequency, buoyancy frequency, topographic slope, and topographic shape.

In Sec. II, we summarize past studies of resonant boundary currents and internal wave generation by tidal flow over two-dimensional topography. Our numerical methods and the details of the parameter variation are described in Sec. III. The results are presented in Sec. IV and are discussed in Sec. V.

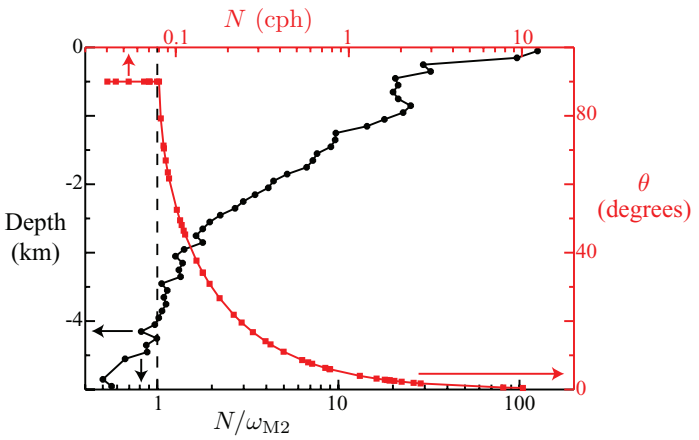

FIG. 1. The local buoyancy frequency $N(z)$ (black circles, black axes on the left and bottom) decreases by more than two orders of magnitude from the shallow ocean down to 5 km depth in the Venezuelan Basin in the Caribbean. The data are taken from cast A22-316N151-4-10 from the World Ocean Circulation Experiment, latitude 13.17° N, longitude 66.00° W, and analyzed (averaging over 50 m depths) by the method described by King *et al.*[11] For depths greater than 4 km, the local buoyancy frequency becomes less than the semi-diurnal lunar tidal frequency ω_{M2} (the black dashed line indicates this *turning depth*). The internal wave angle of propagation, $\theta \equiv \arcsin(\omega/N)$, measured relative to the horizontal and assuming $f = 0$, increases from small values in the shallow ocean where $N \gg \omega$, to 90° in the weakly stratified deep ocean (squares, top and right axes).

II. BACKGROUND

A. Generation of boundary currents and internal tides by critical topography

Cacchione *et al.*[2] observed that the topographic slopes off the coasts of California and New Jersey are approximately equal to the local slopes of internal waves, that is, the topography is critical, $\epsilon = 1$. They suggested that this critical topography resonantly generates intense boundary layer currents that can carry sediment, thus shaping the continental slopes. The resonant generation of boundary currents by critical topography was examined in experimental studies of tidal flow (over a two-dimensional slope) by Zhang *et al.*,[12] who found that at resonance ($\epsilon = 1$) the boundary current velocity was more than an order of magnitude larger than the maximum tidal velocity. At resonance, the measured maximum boundary current velocity was found to vary as L,$^{4/3}$ where L was the length of the topography's near-critical region. For sufficiently large L, the boundary layer currents became unstable and formed Kelvin-Helmholtz billows. The increase in the resonant current with increasing slope length was also observed in numerical studies of Gayen and Sarkar,[13] who also observed that 3D instabilities could occur along the continental slope, resulting in spanwise wave breaking and turbulent mixing.[14,15]

Critical topography has also been identified as being particularly effective in converting tidal motions to internal tides by Lamb.[16] In a review of internal tide generation, Garrett and Kunze[17] argued that intense internal waves would be radiated by slopes near criticality, and these internal waves would lead to local mixing; however, Garrett and Kunze[17] also point out that most of the energy flux is expected to reside in low vertical modes. Griffiths and Grimshaw[18] used a modal decomposition method to argue that there is a resonant forcing of internal waves by critical topography along a continental slope. In similar experimental studies, Lim *et al.*[19] found that intense internal wave beams were radiated only when a critical slope was present along their continental shelf/slope system. Zhang *et al.*[12] and Gayen and Sarkar[13] both also suggested that critical topography leads, in addition to the resonant boundary currents described above, to intense internal waves that propagate away from the continental slope. However, no past work has examined the relationship between the radiated internal wave power and the boundary current intensity as a function of the relevant parameters of the problem.

B. Internal tide generation: Past theoretical studies

Garrett and Kunze[17] have reviewed theoretical approaches to understanding internal tide production. Baines[20] used the method of characteristics, which is broadly applicable yet difficult to implement. Analytical predictions for the internal wave power generated by inviscid tidal flow in two dimensions have been obtained assuming the hydrostatic approximation ($\omega \ll N$), in the limits of weak topography by Bell[21] and steep topography by Llewellyn Smith and Young.[22] Bell[21] predicted that in the limit $\epsilon \to 0$ in an infinitely deep ocean

$$P^{\mathrm{h}}_{\mathrm{Bell}} = \frac{\pi}{8}\rho_0 H^2 A^2 \omega^2 N L_y = \frac{\pi}{8} P_{\mathrm{tide}} \frac{N}{\omega}. \tag{5}$$

This prediction was extended by Llewellyn Smith and Young[23] and Khatiwala[24] to account for finite-depth effects, which were shown to reduce the radiated power. Even though these linear, inviscid theoretical results become singular for critical ($\epsilon = 1$) and supercritical topography ($\epsilon > 1$), Balmforth *et al.*[25] showed that the power radiated by subcritical topography ($\epsilon < 1$) in the deep ocean is proportional to H^2 and smoothly increases only modestly as the topography steepens from Bell's limit of $\epsilon \ll 1$ towards the critical case of $\epsilon = 1$.

To circumvent the singularities that arise for critical and supercritical topography ($\epsilon \geq 1$), Llewellyn Smith and Young[22] used a Green's function approach[26] to compute the conversion of the barotropic tide into the internal tide for knife-edge topography (where $\epsilon \to \infty$)

$$P^{\mathrm{h}}_{\mathrm{LSY}} = \frac{\pi}{4}\rho_0 H^2 A^2 \omega^2 N L_y = \frac{\pi}{4} P_{\mathrm{tide}} \frac{N}{\omega}. \tag{6}$$

Pétrélis *et al.*[27] used the Green's function method to perform hydrostatic calculations that showed the power smoothly varies from Bell's[21] prediction for subcritical topography (Eq. (5)) towards Llewellyn Smith and Young's[22] result for supercritical topography (Eq. (6)). The tidal conversion in the extreme cases of $\epsilon \to \infty$ predicted by Llewellyn Smith and Young[22] and $\epsilon \to 0$ described by Bell[21] only differ by a factor of two. The radiated power shows a similar modest increase as the ratio of the topographic height to the fluid depth approaches unity,[22,28] gaining only a factor of two as this ratio increases from 0 to 0.92 when the scaling with H^2 is taken into account.

These analytical predictions were shown to agree with hydrostatic numerical simulations by di Lorenzo *et al.*,[29] despite the singularities that arise in linear, inviscid analytical calculations for critical and supercritical topography. di Lorenzo *et al.*[29] also highlighted the importance of resolving the topography, as smoothing the topography acted to reduce estimates of the radiated power. This point was emphasized by Zilberman *et al.*,[30] whose model yielded estimates of tidal conversion for the Mid-Atlantic Ridge that decreased by as much as 20% when the topography was smoothed.

A Green's function[26] approach has also been used to predict the power radiated by tidal flow over more complicated topographic structures. An infinite series of evenly spaced knife edges was considered (for an inviscid fluid) by Nycander,[31] who found that the radiated internal wave power depends strongly upon the height and spacing of the ridges, and diverges for particular parameter values. Similarly, Balmforth and Peacock[32] calculated for periodic Gaussian, sinusoidal, and sawtooth topographies the dependence of the power on the height and spacing of the peaks. These two studies of internal wave power radiated by periodic topography showed that estimates of the average radiated power are independent of the height, which is in contrast to the H^2 dependence found for isolated topographic features. The requirement for the topography to be spatially periodic was removed by the studies of Echeverri and Peacock,[33] where the Green's function method was extended to arbitrary two-dimensional topography.

Griffiths and Grimshaw,[18] using modal decomposition, developed a linear, hydrostatic model that enabled them to consider internal tide generation by arbitrary three-dimensional topography for general background stratifications. Zarroug *et al.*[34] instead accounted for nonuniform stratifications using homogenization theory, which was shown to be more appropriate than the WKB approximation for low vertical modes (long vertical wavelength variations). Since the WKB approximation uses the buoyancy frequency at the bottom boundary, the method may underestimate the global tidal conversion because local mixing over the topography can reduce the buoyancy frequency.[31]

C. Internal tide generation: Past experimental and numerical studies

Internal tide generation by two-dimensional topography has also been the focus of a number of experimental and numerical studies. In addition to the aforementioned analytical studies, Khatiwala[24] performed nonhydrostatic numerical simulations of internal tide generation by truncated sine or Gaussian ridges, focusing on finite-depth effects and the variation of the power with the criticality parameter ϵ. Khatiwala[24] found that finite-depth effects can greatly reduce the radiated power for topography that is wide along the direction of the tidal flow (compared to the wavelength of a mode-1 internal wave), and that the radiated power can saturate for certain supercritical topography. The generation of harmonics and wave-breaking by nonlinear beam-beam interactions were simulated for supercritical topography by Lamb.[16] Gostiaux and Dauxois[35] experimentally examined the generation of internal tides by a continental shelf break, which was shown to be analogous to internal wave generation by an oscillating cylinder. Along the same lines, Zhang *et al.*[36] oscillated a cylinder horizontally to experimentally simulate the generation of internal waves by supercritical topography. Their results agreed well with the viscous theoretical predictions of Hurley and Keady[37] in the linear regime, while higher harmonics were generated for stronger forcing. Internal tide generation by knife edge and Gaussian topography was experimentally shown to agree with prior theory by Peacock *et al.*[38] when viscous dissipation, which smoothed the experimental wavefields and suppressed instabilities, was accounted for in the predictions. The modal structure of internal tides generated by Gaussian topography was experimentally and numerically shown by Echeverri *et al.*[39] to agree with linear theory only for small tidal excursions ($\sim$1% of the topographic width), while higher modes were strongly affected for larger tidal excursions. Qian *et al.*[40] performed numerical simulations that showed that the presence of a strong pycnocline above ridges could greatly enhance the radiated internal wave power, even if the stratification in the vicinity of the topography was weak. Lim *et al.*[19] performed experiments of tidal motions over a continental shelf/slope system, which produced internal wave beams only when a critical slope was present, while boluses could form for other parameter values.

D. Nonhydrostatic effects and turning depths

The work discussed above has either been restricted to or primarily focused on situations where the hydrostatic approximation is valid ($\omega \ll N$). Approximately half of the internal wave energy in the ocean is at the semi-diurnal lunar tidal frequency[1,41] ω_{M2}, which is typically much less than characteristic values of the buoyancy frequency in the shallow ocean. In such cases, internal waves propagate nearly horizontally (small S_{IW}) and have small vertical length scales compared to their horizontal extent. Therefore, applying the hydrostatic approximation to study internal tide generation by topography in the shallow ocean or mid-ocean ridges is valid.

The buoyancy frequency, however, decreases by two orders of magnitude or more from the shallow ocean to the abyss (see Fig. 1). King *et al.*[11] analyzed temperature, pressure, and salinity data from the World Ocean Circulation Experiment (WOCE) for thousands of locations throughout the oceans, and they found that the local buoyancy frequency becomes smaller than ω_{M2} for many locations in the deep ocean. Internal waves reflect from turning depths where $N(z) = \omega_{M2}$, and become evanescent (exponentially damped) below.[42,43] The internal wave slope S_{IW} diverges at a turning depth, where the direction of propagation becomes vertical ($\theta \equiv \arcsin(\omega/N)$ reaches 90; see the red curve in Fig. 1). Thus, in the vicinity of a turning depth the hydrostatic approximation fails, as the horizontal length scales are no longer much greater than the vertical length scales, and nonhydrostatic effects on internal tide generation become important.

The analytical predictions of Bell[21] and Llewellyn Smith and Young,[22] given by Eqs. (5) and (6), were derived under the hydrostatic approximation, where the $\sqrt{N^2 - \omega^2}$ term in the Navier-Stokes equation is replaced with N; this is obviously valid for $\omega \ll N$. It has been recognized[17,25,32,33,40] that the analytical predictions of Bell[21] and Llewellyn Smith and Young[22] may be extended to nonhydrostatic cases by maintaining the full $\sqrt{N^2 - \omega^2}$ term in the equations of motion, yielding

the following analytical predictions:

$$P_{\text{Bell}}^{\text{nh}} = \frac{\pi}{8}\rho_0 H^2 A^2 \omega^2 \sqrt{N^2 - \omega^2} L_y = \frac{\pi}{8} P_{\text{tide}} \frac{1}{S_{\text{IW}}}, \tag{7}$$

$$P_{\text{LSY}}^{\text{nh}} = \frac{\pi}{4}\rho_0 H^2 A^2 \omega^2 \sqrt{N^2 - \omega^2} L_y = \frac{\pi}{4} P_{\text{tide}} \frac{1}{S_{\text{IW}}}. \tag{8}$$

For $\omega \ll N$, the nonhydrostatic expressions (7) and (8) reduce to the hydrostatic predictions of Bell[21] and Llewellyn Smith and Young[22] in Eqs. (5) and (6). As in the hydrostatic limit, the power radiated by infinitely steep topography ($\epsilon \to \infty$) is predicted to be twice that predicted for infinitely shallow topography ($\epsilon \to 0$).

For both hydrostatic and nonhydrostatic cases, the radiated internal wave power is predicted to be proportional to the effective tidal power P_{tide} (see Eq. (2)) that interacts with the topography. In the hydrostatic limit, the power is predicted to be proportional to N/ω, while in the nonhydrostatic case the power is predicted to be proportional to the inverse beam slope ($1/S_{\text{IW}}$). Hydrostatic and nonhydrostatic predictions differ particularly for the weak stratifications near a turning depth. As $N \to \omega_{M2}$, hydrostatic theory predicts the internal wave power to be comparable to the tidal power, while nonhydrostatic theory predicts zero radiated power in this case. For the data in Fig. 1, hydrostatic theory overestimates the radiated power by only 3% at a depth of 2 km, but the error increases to 65% at 3 km depth and diverges at the turning depth, 4 km. Therefore, while a topographic ridge with a height $H \sim 1$ km would typically be expected to efficiently convert barotropic tidal motions to internal tides, the radiated power could be significantly decreased in locations in the abyssal oceans where $N \sim \omega_{M2}$.

III. METHODS

We simulate internal wave generation by tidal flow over two-dimensional topography in a uniformly stratified fluid by solving the Navier-Stokes equations in the Boussinesq approximation. The code is CDP 2.4,[44] a parallel, finite-volume-based solver (the subgrid modeling is disabled). Second-order accuracy in space and time is achieved using a fractional-step time-marching scheme and multiple implicit schemes for the spatial operators.[45] The equations are solved for the density ρ, pressure p, and velocity $\boldsymbol{v} = (u, w)$ in the (x, z) directions

$$\frac{\partial \boldsymbol{v}}{\partial t} + (\boldsymbol{v}\cdot\nabla)\boldsymbol{v} = -\frac{1}{\rho_0}\nabla p - \frac{g\rho}{\rho_0}\hat{\boldsymbol{z}} + \nu\nabla^2\boldsymbol{v} + \frac{F_{\text{tide}}}{\rho_0}\hat{\boldsymbol{x}}, \tag{9}$$

$$\nabla\cdot\boldsymbol{v} = 0, \tag{10}$$

$$\partial\rho/\partial t + (\boldsymbol{v}\cdot\nabla)\,\rho = D\nabla^2\rho, \tag{11}$$

where $\rho_0 = 1000$ kg/m^3, $\nu = 0.01$ m^2/s (unless otherwise specified) is the kinematic viscosity, and $D = 2 \times 10^{-5}$ m^2/s is the salt diffusivity, resulting in a Schmidt number of $\nu/D = 500$. We also simulate cases with $\nu = 0.003$ and 0.03 m^2/s and find that the normalized power $\widetilde{P}$ is unchanged, while the resonant boundary currents are enhanced (diminished) for decreasing (increasing) viscosity. The tidal force $F_{\text{tide}} = \rho_0 A\omega^2 \sin\omega t$ produces a velocity $v_{\text{tide}} = -\hat{x}\,A\omega\cos\omega t$, where A is the tidal excursion (A is much less than the topographic width, as in the oceans). We vary the tidal excursion over the range $1 < A < 40$ m, and find less than 10% variation in the measured quantities over this range; the data presented are for $A = 10$ m. To change the criticality parameter and beam slope, we vary the tidal frequency ω for constant buoyancy frequency ($N = 1.55 \times 10^{-4}$ rad/s) or we fix the tidal frequency ($\omega = \omega_{\text{M2}} = 1.4052 \times 10^{-4}$ rad/s) and vary N. This results in typical Reynolds numbers based upon the tidal flow and topographic height of $Re = A\omega H/\nu \sim 10^2$ and topographic Froude numbers of $Fr = A\omega/NH \sim 10^{-2}$. The time step $\Delta t = \pi/1000\omega$ yields 2000 time steps per tidal period. The simulations are run for 15–20 tidal periods, which is sufficient to yield a steady state for at least 5 tidal periods.

TABLE I. Numerical simulation parameters. Here, S_{topo} is the maximum topographic slope, S_{IW} is the slope of the internal wave beam, $\epsilon = S_{\text{topo}}/S_{\text{IW}}$ is the criticality parameter, ω is the tidal frequency, and N is the buoyancy frequency.

Topographic shape	S_{topo}	$1/S_{\text{IW}}$	ϵ	ω (10^{-4} rad/s)	N (10^{-4} rad/s)
Triangular	0.2–11.25	0.18–10	2	0.154–1.526	1.55
Triangular	0.63–11.25	0.18–3.2	2	1.4052	1.11–3.64
Triangular	0.2–2	0.1–1	0.2	1.096–1.542	1.55
Triangular	1	0.1–10	0.1–10	0.154–1.542	1.55
Triangular	$1/\sqrt{3}$	0.17–17	0.1–10	0.089–1.527	1.55
Triangular	2	0.1–5	0.2–10	0.304–1.542	1.55
Gaussian	1	0.2–10	0.2–10	0.154–1.520	1.55
Knife edge	∞	0.14–10	∞	0.154–1.535	1.55
Semicircle	∞	0.2–10	∞	0.154–1.520	1.55

The computational domain, generated with Pointwise Gridgen, spans $-40 < x < 40$ km and $0 < z < 8$ km. Different topographic shapes (described below) are centered at $x = 0$ km with the bottom at $z = 0$ km. The structured grid is composed of rectangular control volumes with smoothly varying spatial resolution. The horizontal resolution along the topography changes from $\Delta x = 10$ m in the center to $\Delta x = 200$ m for $|x| > 35$ km. The boundary layer is resolved using $\Delta z = 0.8$ m for the first 200 m above the topography, and then the resolution is monotonically changed to $\Delta z = 15$ m for $z > 2$ km. The domain has approximately 10^6 control volumes. No-slip boundary conditions are enforced along the upper and lower boundaries, while periodic boundary conditions are used in the x-direction. To mimic an infinitely deep ocean and to minimize finite-size effects, we apply a Rayleigh damping force proportional to the deviation from the tidal velocity ($\propto (\boldsymbol{v} - \boldsymbol{v}_{\text{tide}})$) for $z \geq 5$ km and $|x| \geq 30$ km. Convergence tests with spatial and temporal resolution doubled for $\epsilon = 0.1, 1, 10$ changed the computed velocities by less than 1%, and halving the spatial and temporal resolution changed the velocities by less than 3%.

Simulations are conducted for several symmetric topographies of height $H = 0.5$ km: multiple triangular-shaped ridges, a Gaussian ridge, a knife edge, and a semi-circular topography; see Table I for the range of parameters for each topographic shape. The triangular ridges have constant slope flanks ($0.2 \leq S_{\text{topo}} \leq 11.25$) connected at the peak by a circular cap of radius $r = 62.5$ m and to the bottom by a smooth parabolic curve of height 40 m (see Fig. 2(a)). The Gaussian ridge has $\max(S_{\text{topo}}) = 1$. The knife edge has thickness 16 m and the semi-circle has a radius of 0.5 km.

The internal wave power radiated to the far field is obtained for the triangular, semi-circle, and knife edge topographies by integrating the energy flux along paths with the same shape as the topography; for the Gaussian ridge, we use a triangular-shaped path with flanks of slope 1. The qualitative behavior of the radiated power is insensitive to the choice of path. The integration path for obtaining the energy flux is located at a distance δ from the topography, as illustrated by Fig. 2(a). The radiated power measured through cross-sections of increasing δ for triangular topography with $S_{\text{IW}} = S_{\text{topo}} = 1$ and $\epsilon = 1$ are shown in Fig. 2(b). The radiated power decays rapidly inside the laminar boundary layer ($\delta/H < 0.1$), and then transitions to a gradual decay as the internal wave beam propagates away from the topography ($\delta/H > 0.1$). We therefore choose a value of $\delta = 100$ m, which corresponds to $\delta/H = 0.2$ as shown by the dashed red line in Fig. 2(b), which is outside of the boundary layer yet close enough to the topography so that viscous decay is negligible.

IV. RESULTS

Figure 3 illustrates that resonant boundary currents form over critical topography, but they do not enhance the internal wave power radiated to the far-field. Here, we compare the kinetic energy density and the energy flux in the direction of internal wave propagation ($\Phi_{\text{IW}} \equiv \boldsymbol{\Phi} \cdot \hat{\mathbf{z}}/\sin(\theta)$) for subcritical topography $\epsilon = 1/\sqrt{3}$ (top panels), critical topography $\epsilon = 1$ (middle panels), and supercritical topography $\epsilon = 2$ (bottom panels) with $S_{\text{IW}} = 1$. Critical topography generates resonant boundary currents, as observed in prior studies.[2,12–15] However, the resonant boundary currents and

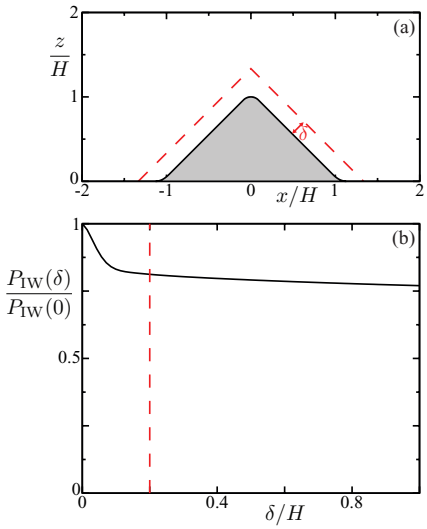

FIG. 2. (a) The radiated internal wave power is obtained by integrating the energy flux normal to a cross-section (dashed line) that is a distance δ from the topography (gray). The triangular topography here has slope $S_{\mathrm{topo}} = 1$ and $\delta = 100$ m. (b) The power P_{IW} radiated through a cross-section a distance δ away from the topography reveals the decay of the internal waves as they propagate away from the topography. (Triangular topography with $S_{\mathrm{IW}} = S_{\mathrm{topo}} = 1$ and $\epsilon = 1$.)

strong kinetic energy density present in the internal wave beams for the critical case do not lead to enhanced internal wave power radiating to the far-field. This observation is further emphasized in Sec. IV A. While increasing the criticality parameter from $\epsilon = 1$ to $\epsilon = 2$ is expected to increase the radiated power, we demonstrate below that the radiated power scales more strongly with the beam slope, especially in the vicinity of a turning depth (see red curve in Fig. 1).

A. Relation of boundary currents to radiated wave power

We examine the connection between the boundary currents and the tidal conversion by computing both the integrated kinetic energy density in the boundary currents, as in Zhang *et al.*,[12] and the power radiated to the far-field. The spatially- and tidally averaged kinetic energy density $K = (2\mathcal{A}_{\mathrm{box}})^{-1} \int\int \rho_0 \langle \boldsymbol{v}^2 \rangle \, \mathrm{d}x\mathrm{d}z$ is computed for a region within a box centered on the linear part of the tent topography; the box has half of the length of the slope and extends outward 100 m away from the topography. Figure 4(a) shows the normalized kinetic energy density $\widetilde{K} = K/K_{\mathrm{tide}}$, where $K_{\mathrm{tide}} = \rho_0 A^2 \omega^2/4$ is the average tidal kinetic energy density. For $\epsilon < 1$, $\widetilde{K}$ is dominated by barotropic tidal motions, resulting in normalized values near unity. For critical topography ($\epsilon = 1$), there is a resonant peak, as found in prior studies.[12–15] At higher values of ϵ, the internal waves block the tidal motions near the topography, resulting in vanishing boundary currents.

The resonant peak for the boundary current kinetic energy density is enhanced (diminished) by decreasing (increasing) the fluid viscosity, which acts to increase (decrease) the Reynolds number of the flow. The resonant peak also increases as the topographic length is increased. In the laboratory experiments of Zhang *et al.*,[12] which were at higher Reynolds numbers than we simulated here, the kinetic energy density was found to be approximately 60 times the maximum tidal kinetic energy density. These experimental observations were complemented by numerical studies by Gayen and Sarkar,[13] who focused on the scaling with the slope length. The Reynolds numbers of oceanic flows far exceed those achieved in these past studies as well as the work presented here, indicating that the resonant boundary currents can be significantly stronger in the ocean.[2]

While the boundary currents are strongest near $\epsilon = 1$, the internal wave power monotonically increases with the criticality parameter, as Fig. 4(b) illustrates. We multiply $\widetilde{P}$ by the inverse beam slope to account for the scaling predicted by the nonhydrostatic versions of Bell's and Llewellyn Smith and Young's theories, given by Eqs. (7) and (8), which allows us to focus on changes resulting

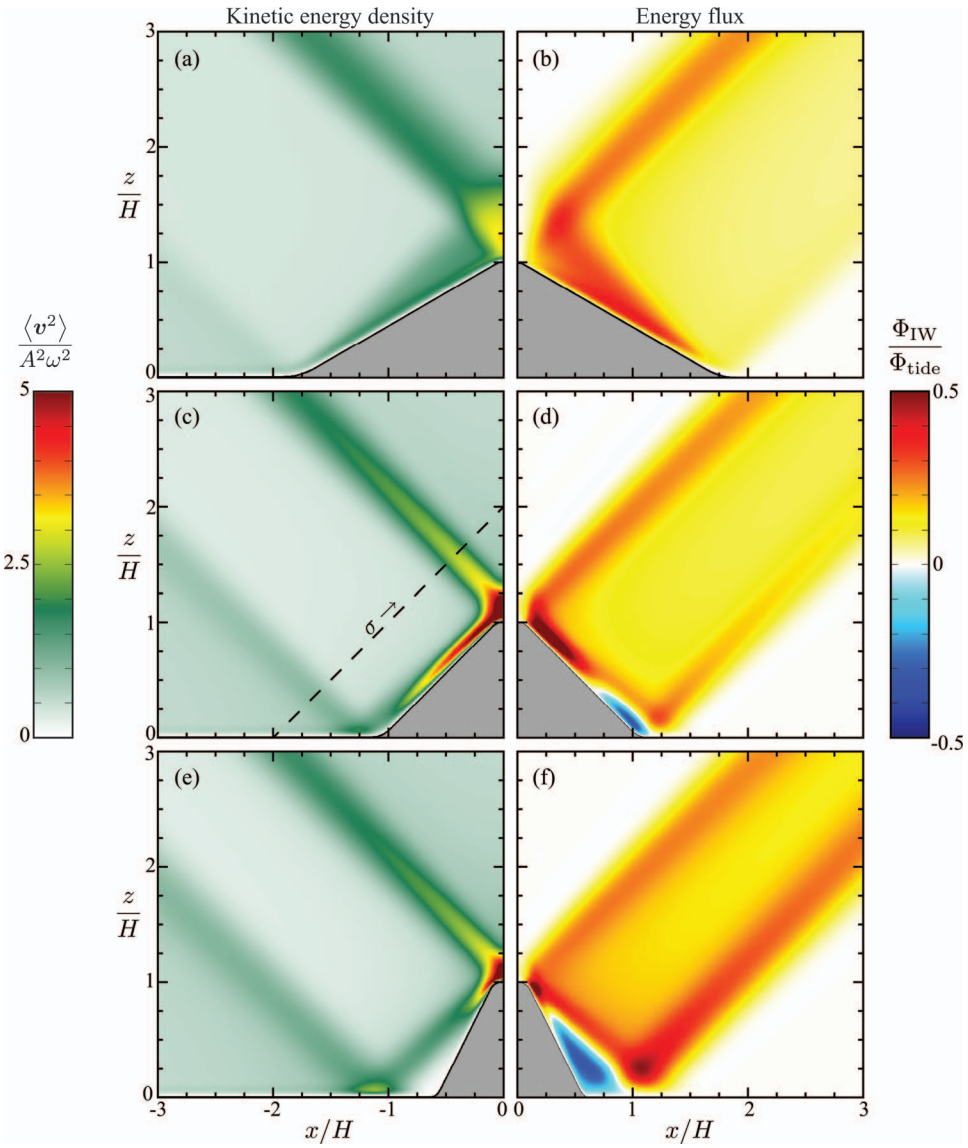

FIG. 3. Strong boundary currents form for critical topography ($\epsilon = 1$), (c) and (d), while the radiated internal waves are stronger for supercritical topography ($\epsilon = 2$), (e) and (f). Subcritical topography ($\epsilon = 1/\sqrt{3}$) (a) and (b) is also shown for comparison. The tidally averaged kinetic energy density on the left reveals the boundary currents, while the tidally averaged energy flux in the direction of the internal wave beams, Φ_{IW}/Φ_{tide} (defined in Sec. IV), is on the right. In Fig. 5, we compare the kinetic energy density and beam flux measured at the cross-section indicated by black dashed line in (c).

from varying the criticality parameter. While there is no resonant peak in the power radiated by critical topography, we do observe a transition in behavior at $\epsilon \approx 1$. Unlike the resonant boundary currents, no change in the radiated power is observed for different viscosities, and we note that our measurements for large and small ϵ approach the predictions of *inviscid* linear theory.

Direct measurements of the energy flux of internal wave beams are rare in laboratory experiments and oceanic measurements because of the difficulty in determining the pressure field. As an alternative, the kinetic energy density is often used to characterize the strength of radiated internal waves. Figure 5 compares the kinetic energy density and energy flux for the critical and supercritical topography shown in Figs. 3(c)–3(f). Values of the kinetic energy density for the top internal wave beams (near $\sigma/H = 2.2$) are higher than for the beams that initially propagate downward and reflect from the bottom boundary (peaked near $\sigma/H = 0.6$). Further, the kinetic energy density is largest for

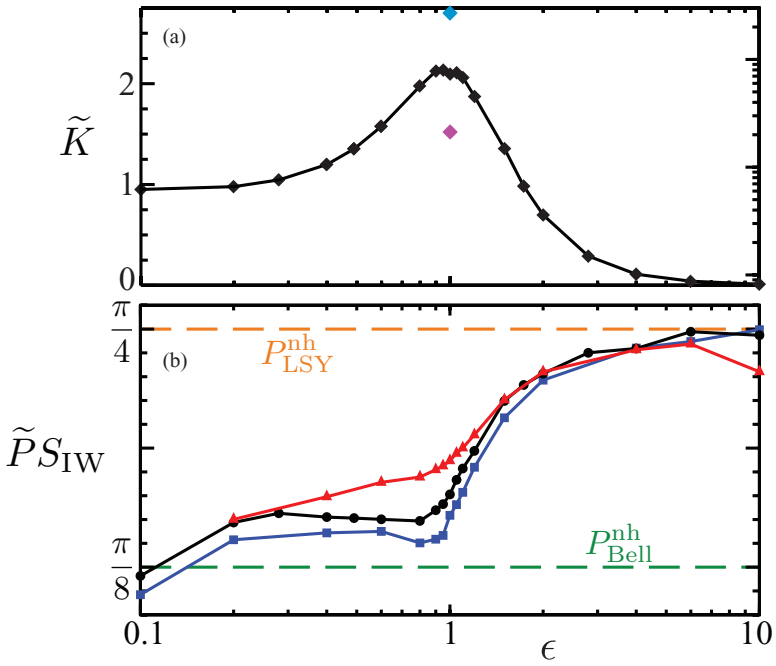

FIG. 4. (a) Resonant boundary currents form for tidal flow over triangular topography ($S_{\rm topo} = 1$) near criticality ($\epsilon \approx 1$), as revealed by the peak in $\widetilde{K}$, which is the spatially- and time-averaged kinetic energy density normalized by the average tidal kinetic energy density (see text). The peak at $\epsilon = 1$ is higher (lower) for smaller (larger) viscosity, as shown by the blue diamond for viscosity 70% smaller, and a red diamond for viscosity 3 times larger. However, changing the viscosity does not change the radiated power (not shown). (b) The dependence of the normalized power $\widetilde{P}$ (multiplied by $1/S_{\rm IW}$) is shown for triangular topography with slopes $S_{\rm topo} = 1/\sqrt{3}$ (squares), $S_{\rm topo} = 1$ (black circles), and $S_{\rm topo} = 2$ (triangles). $\widetilde{P}$ exhibits a transition for $\epsilon \approx 1$; below the transition the nonhydrostatic extension of Bell's theory (lower dashed line, Eq. (7)) gives a lower bound, and above the transition the nonhydrostatic extension of Llewellyn Smith and Young's theory (upper dashed line, Eq. (8)) gives an upper bound.

the internal wave beam generated by critical topography. However, the behavior of the energy flux is different. The peak value of the energy flux corresponds to the internal wave beam generated by supercritical topography that reflects off of the bottom boundary (peak in Fig. 5(b) near $\sigma/H = 0.8$). While this internal wave beam yields the largest values of energy flux and radiated power, the kinetic energy density only has a modest peak compared to the others that did not reflect from the bottom boundary. The kinetic energy density in the area between the peaks of the internal wave beams ($1 < \sigma/H < 2$) is very similar for critical and supercritical topography, although the energy flux in the supercritical case is higher over this entire range. Finally, the largest peak in the kinetic energy density ($\sigma/H \approx 2.2$) of critical topography does correspond to a maximum in the energy flux, but this is not the case for supercritical topography. We therefore conclude that the kinetic energy density should not be used as a proxy for the energy flux to characterize the conversion of tidal motions to internal waves, as the two quantities do not have a consistent relationship.

B. Radiated power dependence on beam slope

Many of the prior studies described in Sec. II focused on the scaling of the radiated power with the criticality parameter, topographic height, and the ratio of the topographic height to the total fluid depth. In the deep ocean, the internal wave beam slope increases rapidly with depth, particularly in the vicinity of a turning depth where it diverges (cf. Fig. 1). We now examine the scaling of the radiated power with beam slope for cases where the hydrostatic approximation is valid and for cases where the approximation fails.

The normalized power $\widetilde{P}$ radiated by tidal flow over triangular topography with fixed criticality parameter is independent of whether the beam slope is changed by varying ω or N, as Fig. 6(a)

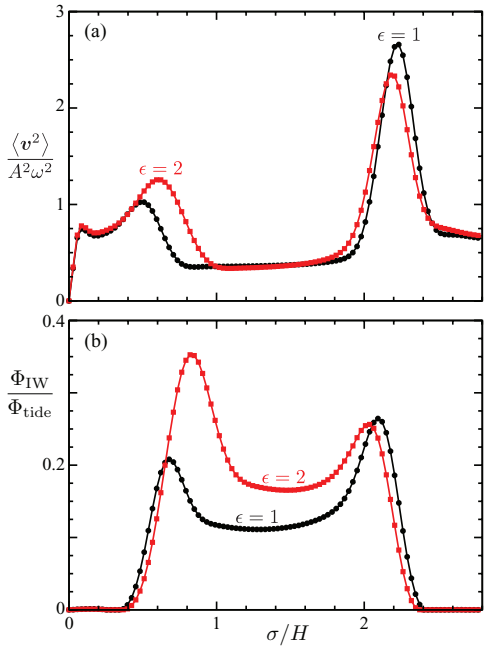

FIG. 5. A comparison of the tidally averaged (a) kinetic energy density and (b) energy flux in the direction of the internal wave beams for the critical topographies (black circles) and supercritical topographies (squares) shown in Figs. 3(c)–3(f). The measurements are taken along a cross-section from ($x/H = -2$, $z/H = 0$) to ($x/H = 0$, $z/H = 2$), which is shown as the dashed line in panel (c) of Fig. 3.

illustrates. As a matter of convenience, we fix the stratification and vary the tidal frequency in the subsequent parameter variations.

We first compare our measurements to the hydrostatic theories of Bell[21] (Eq. (5)) and Llewellyn Smith and Young[22] (Eq. (6)), which are also shown in Fig. 6(a). As expected, the theories fail to predict the power for small inverse beam slopes ($1/S_{IW} < 1$), which correspond to cases with weak stratification where $\omega \to N$. Our measurements indicate that the power is inversely proportional to the beam slope for all S_{IW}. While $\widetilde{P}$ approaches a constant for the hydrostatic theories at small

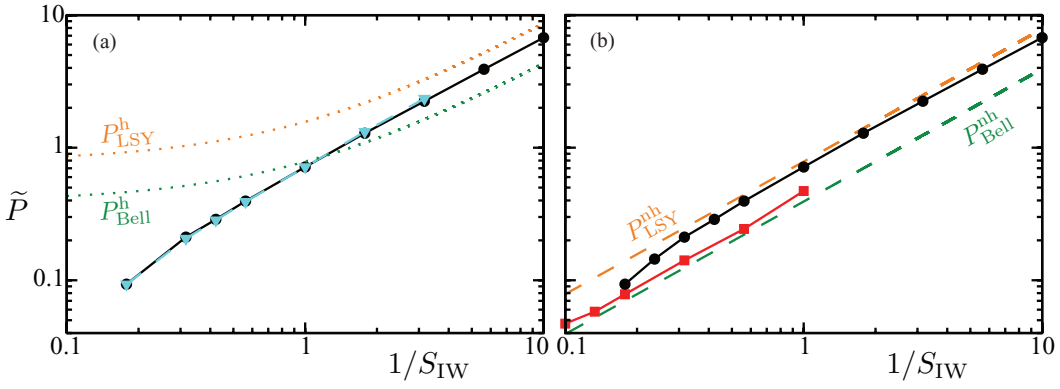

FIG. 6. (a) The normalized radiated power $\widetilde{P}$ for triangular topography increases linearly with inverse beam slope $1/S_{IW}$, both for varying tidal frequency ω (black circles) with N fixed (1.55×10^{-4} rad/s) and for varying N (triangles) with ω fixed (1.4052×10^{-4} rad/s); $\epsilon = 2$. Dotted lines show the hydrostatic theories of Bell[21] (lower line) and Llewellyn Smith and Young[22] (upper line), given by Eqs. (5) and (6). (b) The nonhydrostatic extensions (dashed lines) of the theories (lower line, Eq. (7)) and (upper line, Eq. (8)) exhibit the observed dependence of the radiated power on $1/S_{IW}$, and provide bounds for the dependence on ϵ. (Triangular topography with $\epsilon = 2$ (black circles) and $\epsilon = 0.2$ (squares).)

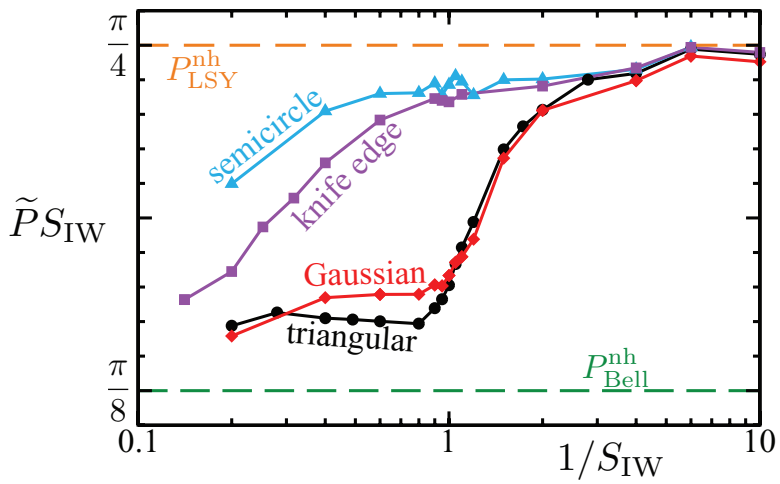

FIG. 7. The normalized power $\widetilde{P}$ compensated by $1/S_{\mathrm{IW}}$ radiated by topography of different shapes is bounded by the nonhydrostatic extensions (dashed lines) of the theories of Bell[21] (lower line) and Llewellyn Smith and Young[22] (upper line), given by Eqs. (7) and (8).

values of inverse beam slope, nonhydrostatic effects reduce the power relative to the hydrostatic predictions.

The nonhydrostatic extensions of the theories of Bell[21] and Llewellyn Smith and Young,[22] given by Eqs. (7) and (8), each predict $P \propto 1/S_{\mathrm{IW}}$ for all S_{IW}, in accord with our measurements in Fig. 6(a). Analogous to the hydrostatic simulations of Pétrélis *et al.*,[27] the nonhydrostatic prediction of Bell's theory agrees well with our simulations for small ϵ, while the nonhydrostatic version of Llewellyn Smith and Young's theory yields accurate predictions at large ϵ, as Fig. 6(b) illustrates. For supercritical topography with very steep beam slopes ($1/S_{\mathrm{IW}} < 0.3$), we find that the radiated power begins to decrease owing to interactions between the internal waves generated on the left- and right-hand sides of the topography.

C. Dependence on topographic shape

Thus far we have considered the internal tidal power radiated by triangular topography with constant slope flanks. This is certainly an idealization of rough ocean topography, which is characterized by many different slope angles and length scales. To extend beyond such simple topography, we compare the results for triangular topography (slope $S_{\mathrm{topo}} = 1$) to the results for Gaussian, knife-edge, and semi-circular ridges in Fig. 7, thus including cases where the slope smoothly varies over a fixed range (Gaussian), is infinitely steep (knife edge), or spans $0 < S_{\mathrm{topo}} < \infty$ (semi-circle). For internal waves with a shallow slope (large $1/S_{\mathrm{IW}}$), the radiated power in all cases approaches the nonhydrostatic prediction of Llewellyn Smith and Young,[22] given by Eq. (8). For steep beam slopes (small $1/S_{\mathrm{IW}}$), the radiated power slowly tends toward the prediction of the nonhydrostatic extension of the Bell theory. Thus, the nonhydrostatic theories are capable of predicting the radiated power for topography with varying slope angles, in addition to the simple triangular topography discussed above.

The results for Gaussian and triangular ridges with the same maximum slope ($S_{\mathrm{topo}} = 1$) are very similar, indicating that using the maximum topographic slope to determine the criticality parameter is appropriate. For shallow beams, the knife-edge and semi-circular topographies yield results similar to those for the Gaussian and triangular ridges, as all of the topographic shapes are supercritical. The decrease in power with increasing beam slope, though, is slower for the knife-edge and semi-circular topographies owing to their steeper topographic slopes.

One would expect the power radiated by the knife-edge to closely agree with $P^{\mathrm{nh}}_{\mathrm{LSY}}$ for all S_{IW}, since this was the case examined theoretically by Llewellyn Smith and Young.[22] However, since their

analytical studies were inviscid and hydrostatic, the internal waves were very thin and propagated at very shallow angles, thus eliminating any interactions between the beams produced from the left- and right-hand sides of the knife edge. In our case though, all four internal wave beams spatially overlap for steep beam angles, which reduces the radiated power below even the nonhydrostatic extension of Llewellyn Smith and Young's[22] theory. The semi-circular ridge radiates more power than the knife edge for steep beams, as the semi-circular topography is much wider, which decreases the spatial overlap and interaction between the internal wave beams. One might expect that semi-circular and Gaussian topography would radiate comparable internal wave power owing to their smooth, continuously varying slopes. However, the maximum topographic slope of the semi-circle is infinite, resulting in radiated powers comparable to the knife-edge, while the maximum slope of the Gaussian topography is equal to that of the triangular topography, resulting in comparable radiated power over the range of beam slopes (cf. Fig. 7).

V. DISCUSSION

Our simulations show that critical topography generates resonant boundary currents, as found in prior studies.[2,12–15] However, this resonance phenomenon does not extend to radiated internal waves that propagate away from the topography. Prior studies have found that this resonance behavior can produce boundary currents that are strong enough to undergo shear instability, leading to turbulence and local mixing,[12–15] which can actually *reduce* the radiated internal wave power rather than enhancing it. Therefore, the turbulence produced by unstable resonant boundary currents over critical topography in the ocean may actually *decrease* the internal wave generation, in contrast to the notion that critical topography generates intense internal waves.

We have also found that the kinetic energy density and radiated internal wave power are largely decoupled. Decreasing (increasing) the viscosity leads to an increase (decrease) in the kinetic energy density of the resonant boundary currents, while the radiated internal wave power remains almost unchanged. Even though the viscous effects in our simulations are stronger than in the ocean, we believe that the decoupling of boundary current kinetic energy density and the radiated power extends beyond our parameter values. Indeed, our measurements of the radiated power agree quantitatively with the *inviscid* theoretical predictions of Bell[21] and Llewellyn Smith and Young[22] for both small and large values of the criticality parameter. Viscous effects are minor in our simulations because we examine the radiated power in the region immediately beyond the laminar boundary layer, whereas experimental studies of internal wave beams farther away from the topography found that viscous effects had to be taken into account.[19,38,39] Future studies could bridge the gap between our focus on varying parameters over wide ranges and the studies that have examined higher Reynolds numbers where the boundary currents become turbulent.[12–15,46]

In summary, the power radiated by internal waves produced by tidal flow over two-dimensional ridges in a uniformly stratified fluid can be described by

$$P = P_{\text{tide}} \frac{1}{S_{\text{IW}}} f(\epsilon, \text{shape}), \tag{12}$$

where $\pi/8 \leq f(\epsilon, \text{shape}) \leq \pi/4$ depends upon the details of the topography and is bounded by the nonhydrostatic versions of the linear, inviscid theories of Bell[21] and Llewellyn Smith and Young.[22] From Eq. (12), we see that variations in the criticality parameter ϵ can only change the power by a factor of two, whereas the power scales as the inverse of the beam slope. This scaling with the beam slope holds for cases where the hydrostatic approximation is appropriate as well as situations where it fails. The beam slope becomes large in the deep ocean, as observed in the Bay of Biscay by Pingree and New,[47] and even diverges if there is a turning depth.[42,43] The nonhydrostatic effects that arise from weak stratifications reduce the radiated power below hydrostatic estimates; this should be considered in making global estimates of the internal wave power radiated by deep ocean topography.

The present work has examined two-dimensional laminar tidal flow over smooth topography in uniformly stratified fluids. However, in the ocean the topography is rough and three-dimensional, and the fluid is not uniformly stratified.[11] Holloway and Merrifield[48] performed three-dimensional hydrostatic simulations of tidal motions over steep topographic features and found that the tidal

conversion strongly increased when the length of the topography orthogonal to the tidal flow increased, which forced the flow to cross isobaths rather than flowing around the topography. While two-dimensional studies can serve as a foundation for understanding tidal conversion by topographic features that efficiently convert tidal motions to radiated internal waves, the effects of three-dimensionality cannot be neglected. Tidal conversion has been examined in three-dimensional simulations of the effects of corrugations in a continental slope, for both cross- and along-slope tidal forcing.[49,50] Studies of tidal flow over a half sphere revealed both a mean flow and an oscillatory flow (at twice the tidal frequency) orthogonal to the tidal direction.[51] Along similar lines, King *et al.*[52] found that tidal motions over a three-dimensional Gaussian mountain produced internal wave beams (at twice the tidal frequency) that propagated orthogonal to the tidal direction, but only when the topography was supercritical. Gayen and Sarkar[14] observed three-dimensional instabilities produced by resonant boundary currents over two-dimensional critical topography. It will be interesting in the future to search for resonant boundary currents in tidal flow over three-dimensional topography.

ACKNOWLEDGMENTS

We thank Likun Zhang, Bruce Rodenborn, Philip Morrison, and Robert Moser for helpful discussions. The computations were done at the Texas Advanced Computing Center. The research was supported by the Office of Naval Research (ONR) MURI Grant No. N000141110701.

[1] W. Munk and C. Wunsch, "Abyssal recipes II: Energetics of tidal and wind mixing," Deep-Sea Res., Part I **45**, 1977–2010 (1998).
[2] D. A. Cacchione, L. F. Pratson, and A. S. Ogston, "The shaping of continental slopes by internal tides," Science **296**, 724–727 (2002).
[3] J. N. Moum, D. R. Caldwell, J. D. Nash, and G. D. Gunderson, "Observations of boundary mixing over the continental slope," J. Phys. Oceanogr. **32**, 2113–2130 (2002).
[4] J. D. Nash, E. Kunze, J. M. Toole, and R. W. Schmitt, "Internal tide reflection and turbulent mixing on the continental slope," J. Phys. Oceanogr. **34**, 1117–1134 (2004).
[5] R. G. Lueck and T. D. Mudge, "Topographically induced mixing around a shallow seamount," Science **276**, 1831–1833 (1997).
[6] E. Kunze and J. M. Toole, "Tidally driven vorticity, diurnal shear, and turbulence atop Fieberling Seamount," J. Phys. Oceanogr. **27**, 2663–2693 (1997).
[7] D. L. Rudnick, T. J. Boyd, R. E. Brainard, G. S. Carter, G. D. Egbert, M. C. Gregg, P. E. Holloway, J. M. Klymak, E. Kunze, C. M. Lee, M. D. Levine, D. S. Luther, J. P. Martin, M. A. Merrifield, J. N. Moum, J. D. Nash, R. Pinkel, L. Rainville, and T. B. Sanford, "From tides to mixing along the Hawaiian Ridge," Science **301**, 355–358 (2003).
[8] J. M. Klymak, J. N. Moum, J. D. Nash, E. Kunze, J. B. Girton, G. S. Carter, C. M. Lee, T. B. Sanford, and M. C. Gregg, "An estimate of tidal energy lost to turbulence at the Hawaiian Ridge," J. Phys. Oceanogr. **36**, 1148–1164 (2006).
[9] K. L. Polzin, J. M. Toole, J. R. Ledwell, and R. W. Schmitt, "Spatial variability of turbulent mixing in the abyssal ocean," Science **276**, 93–96 (1997).
[10] L. C. St Laurent, J. M. Toole, and R. W. Schmitt, "Buoyancy forcing by turbulence above rough topography in the abyssal Brazil Basin," J. Phys. Oceanogr. **31**, 3476–3495 (2001).
[11] B. King, M. Stone, H. P. Zhang, T. Gerkema, M. Marder, R. B. Scott, and H. L. Swinney, "Buoyancy frequency profiles and internal semidiurnal tide turning depths in the oceans," J. Geophys. Res., [Oceans] **117**, C04008, doi:10.1029/2011JC007681 (2012).
[12] H. P. Zhang, B. King, and H. L. Swinney, "Resonant generation of internal waves on a model continental slope," Phys. Rev. Lett. **100**, 244504 (2008).
[13] B. Gayen and S. Sarkar, "Direct and large-eddy simulations of internal tide generation at a near-critical slope," J. Fluid Mech. **681**, 48–79 (2011).
[14] B. Gayen and S. Sarkar, "Turbulence during the generation of internal tide on a critical slope," Phys. Rev. Lett. **104**, 218502 (2010).
[15] B. Gayen and S. Sarkar, "Boundary mixing by density overturns in an internal tidal beam," Geophys. Res. Lett. **38**, L14608, doi:10.1029/2011GL048135 (2011).
[16] K. G. Lamb, "Nonlinear interaction among internal wave beams generated by tidal flow over supercritical topography," Geophys. Res. Lett. **31**, L09313, doi:10.1029/2003GL019393 (2004).
[17] C. Garrett and E. Kunze, "Internal tide generation in the deep ocean," Annu. Rev. Fluid Mech. **39**, 57–87 (2007).
[18] S. D. Griffiths and R. H. J. Grimshaw, "Internal tide generation at the continental shelf modeled using a modal decomposition: Two-dimensional results," J. Phys. Oceanogr. **37**, 428–451 (2007).
[19] K. Lim, G. N. Ivey, and N. L. Jones, "Experiments on the generation of internal waves over continental shelf topography," J. Fluid Mech. **663**, 385–400 (2010).
[20] P. Baines, "The generation of internal tides by flat-bump topography," Deep-Sea Res. Oceanogr. Abstr. **20**, 179–205 (1973).
[21] T. H. Bell, Jr., "Topographically generated internal waves in the open ocean," J. Geophys. Res. **80**, 320–327, doi:10.1029/JC080i003p00320 (1975).

[22] S. G. Llewellyn Smith and W. R. Young, "Tidal conversion at a very steep ridge," J. Fluid Mech. **495**, 175–191 (2003).
[23] S. G. Llewellyn Smith and W. R. Young, "Conversion of the barotropic tide," J. Phys. Oceanogr. **32**, 1554–1566 (2002).
[24] S. Khatiwala, "Generation of internal tides in an ocean of finite depth: Analytical and numerical calculations," Deep-Sea Res., Part I **50**, 3–21 (2003).
[25] N. J. Balmforth, G. R. Ierley, and W. R. Young, "Tidal conversion by subcritical topography," J. Phys. Oceanogr. **32**, 2900–2914 (2002).
[26] R. Robinson, "The effects of a vertical barrier on internal waves," Deep-Sea Res. Oceanogr. Abstr. **16**, 421–429 (1969).
[27] F. Pétrélis, S. G. Llewellyn Smith, and W. R. Young, "Tidal conversion at a submarine ridge," J. Phys. Oceanogr. **36**, 1053–1071 (2006).
[28] L. St Laurent, S. Stringer, C. Garrett, and D. Perraultjoncas, "The generation of internal tides at abrupt topography," Deep-Sea Res., Part I **50**, 987–1003 (2003).
[29] E. di Lorenzo, W. R. Young, and S. G. Llewellyn Smith, "Numerical and analytical estimates of M2 tidal conversion at steep oceanic ridges," J. Phys. Oceanogr. **36**, 1072–1084 (2006).
[30] N. V. Zilberman, J. M. Becker, M. A. Merrifield, and G. S. Carter, "Model estimates of M2 internal tide generation over Mid-Atlantic Ridge topography," J. Phys. Oceanogr. **39**, 2635–2651 (2009).
[31] J. Nycander, "Tidal generation of internal waves from a periodic array of steep ridges," J. Fluid Mech. **567**, 415–432 (2006).
[32] N. J. Balmforth and T. Peacock, "Tidal conversion by supercritical topography," J. Phys. Oceanogr. **39**, 1965–1974 (2009).
[33] P. Echeverri and T. Peacock, "Internal tide generation by arbitrary two-dimensional topography," J. Fluid Mech. **659**, 247–266 (2010).
[34] M. Zarroug, J. Nycander, and K. Döös, "Energetics of tidally generated internal waves for nonuniform stratification," Tellus, Ser. A **62**, 71–79 (2010).
[35] L. Gostiaux and T. Dauxois, "Laboratory experiments on the generation of internal tidal beams over steep slopes," Phys. Fluids **19**, 028102 (2007).
[36] H. P. Zhang, B. King, and H. L. Swinney, "Experimental study of internal gravity waves generated by supercritical topography," Phys. Fluids **19**, 096602 (2007).
[37] D. G. Hurley and G. Keady, "The generation of internal waves by vibrating elliptic cylinders. Part 2. Approximate viscous solution," J. Fluid Mech. **351**, 119–138 (1997).
[38] T. Peacock, P. Echeverri, and N. J. Balmforth, "An experimental investigation of internal tide generation by two-dimensional topography," J. Phys. Oceanogr. **38**, 235–242 (2008).
[39] P. Echeverri, M. R. Flynn, K. B. Winters, and T. Peacock, "Low-mode internal tide generation by topography: An experimental and numerical investigation," J. Fluid Mech. **636**, 91–108 (2009).
[40] H. Qian, P.-T. Shaw, and D. S. Ko, "Generation of internal waves by barotropic tidal flow over a steep ridge," Deep-Sea Res., Part I **57**, 1521–1531 (2010).
[41] C. Wunsch and R. Ferrari, "Vertical mixing, energy and the general circulation of the oceans," Annu. Rev. Fluid Mech. **36**, 281–314 (2004).
[42] Y. V. Kistovich and Y. D. Chashechkin, "Linear theory of the propagation of internal wave beams in an arbitrarily stratified liquid," J. Appl. Mech. Tech. Phys. **39**, 729–737 (1998).
[43] M. S. Paoletti and H. L. Swinney, "Propagating and evanescent internal waves in a deep ocean model," J. Fluid Mech. **706**, 571–583 (2012).
[44] F. Ham and G. Iaccarino, "Energy conservation in collocated discretization schemes on unstructured meshes," *Annual Research Briefs* (Center for Turbulence Research, Stanford, CA, 2004), pp. 3–14.
[45] F. Ham, K. Mattsson, and G. Iaccarino, "Accurate and stable finite volume operators for unstructured flow solvers," *Annual Research Briefs* (Center for Turbulence Research, Stanford, CA, 2006), pp. 243–261.
[46] N. R. Rapaka, B. Gayen, and S. Sarkar, "Tidal conversion and turbulence at a model ridge: Direct and large eddy simulations," J. Fluid Mech. **715**, 181–209 (2013).
[47] R. D. Pingree and A. L. New, "Abyssal penetration and bottom reflection of internal tidal energy in the Bay of Biscay," J. Phys. Oceanogr. **21**, 28–39 (1991).
[48] P. E. Holloway and M. A. Merrifield, "Internal tide generation by seamounts, ridges, and islands," J. Geophys. Res. **104**, 25937–25952, doi:10.1029/1999JC900207 (1999).
[49] S. Legg, "Internal tides generated on a corrugated continental slope. Part I: Cross-slope barotropic forcing," J. Phys. Oceanogr. **34**, 156–173 (2004).
[50] S. Legg, "Internal tides generated on a corrugated continental slope. Part II: Along-slope barotropic forcing," J. Phys. Oceanogr. **34**, 1824–1838 (2004).
[51] B. King, H. P. Zhang, and H. L. Swinney, "Tidal flow over three-dimensional topography in a stratified fluid," Phys. Fluids **21**, 116601 (2009).
[52] B. King, H. P. Zhang, and H. L. Swinney, "Tidal flow over three-dimensional topography generates out-of-forcing-plane harmonics," Geophys. Res. Lett. **37**, L14606, doi:10.1029/2010GL043221 (2010).